Research Square

Preprints are preliminary reports that have not undergone peer review.
They should not be considered conclusive, used to inform clinical practice,
or referenced by the media as validated information.

The Attitude Fingerprint Information Analysis of Space Debris with Photometric Light Curves

Yan Wen
Xian Institute of Optics and Precision Mechanics
Dalei Yao
YaoDalei@yeah.net
Xian Institute of Optics and Precision Mechanics
Fan Bu
Xian Institute of Optics and Precision Mechanics
Yongqing Yang
Xian Institute of Optics and Precision Mechanics
Rongli Chen
Xian Institute of Optics and Precision Mechanics

Article

Keywords: Space debris, Photometric light curves, Attitude fingerprint information, Shapelets, Neural networks

Posted Date: April 30th, 2026

DOI: https://doi.org/10.21203/rs.3.rs-9273518/v1

License: This work is licensed under a Creative Commons Attribution 4.0 International License.
Read Full License

Additional Declarations: No competing interests reported.

The Attitude Fingerprint Information Analysis of Space Debris with Photometric Light Curves

Yan Wen[1], Dalei Yao[1,*], Fan Bu[1], Yongqing Yang [1,2], Rongli Chen[1]

[1]Xi'an Institute of Optics and Precision Mechanics, Xi'an, 710119, China

[2]Northwestern Polytechnical University, Xi'an, 710119, China

Correspondence: YaoDalei@yeah.net

Abstract

To address the challenge of directly observing the attitude fingerprint information of space debris, this paper investigates the problem of extracting attitude-related information of space debris from photometric light curves. A framework named Photometric Light Curve Attitude Fingerprint Network (PAFNet) is proposed to link simulated photometric data with data-driven feature analysis. First, a photometric simulation model that incorporates geometric structure, orbital motion, and surface reflection properties is developed to generate light curves under controlled conditions. Second, a feature extraction method combining Shapelets and neural networks is designed to capture both local temporal patterns and global characteristics of the light curves. Finally, an attitude inversion approach based on photometric matching and a genetic algorithm is employed to estimate attitude parameters by comparing observed and simulated light curves. Experimental results show that the proposed method can recover attitude parameters with reasonable accuracy under varying noise levels and limited observation lengths. Additional analysis indicates that smoothing preprocessing and the use of multiple light curves can improve the stability of the inversion results.

Keywords: Space debris; Photometric light curves; Attitude fingerprint information; Shapelets; Neural networks.

1. Introduction

As the number of on-orbit objects in Earth's orbit continues to increase, the space debris problem is increasingly serious [1]. A large number of failed spacecrafts, rocket debris, and fragments generated by their collisions pose a serious threat to the long-term safe operation of on-

orbit spacecraft. To improve space situational awareness, refined characterization of space debris is important in target monitoring [2]. Space debris has complex and diverse shapes and structures, especially small debris, which is more difficult to identify and track. In addition to orbital information, the attitude state and evolution characteristics of debris are of great significance in collision risk assessment, on-orbit servicing, and active cleanup missions. However, space debris is usually a non-cooperative target, and its attitude information is difficult to obtain through direct observation. Existing radar and optical imaging methods both have certain limitations in attitude inversion: radar observation has all-weather capability, but its resolution is limited in high-precision attitude reconstruction; optical imaging methods rely on high-resolution equipment and are easily constrained by observation conditions and cost. Therefore, exploring attitude inversion methods based on indirect observation data is of significant research value.

Photometric light curves [3], as a typical form of passive optical observation data, have been widely used in space debris monitoring. When space debris is illuminated by sunlight, its surface reflectivity fluctuates with its attitude, resulting in light variation curves with time-series characteristics. This type of data contains information about the debris's spin period, attitude change patterns, and surface structure, providing a potential basis for attitude inversion. However, light variation curves are typically characterized by strong non-stationarity, significant noise interference, and interwoven multi-scale features, making it difficult for traditional methods based on empirical features or simplified models to accurately characterize complex attitudes.

Furthermore, photometric data [4] is inherently a highly integrated information carrier, containing not only target attitude information but also being influenced by target shape, material, surface reflectivity, and observation geometry. This multi-factor coupling makes separating pure attitude information from photometric data a highly challenging task. For example, debris with different shapes or surface properties may produce similar light variation curves, increasing the uncertainty of the inversion. On the other hand, actual observational data typically exhibits characteristics of "short arcs" and "high noise." For low-Earth orbit (LEO) objects, their relatively high-speed relative to ground-based observation stations limits visibility to only a few minutes, making it difficult to obtain continuous, long-term photometric sequences [5]. For medium- and high-Earth orbit (MEO) objects, while visibility is relatively longer, it is still constrained by weather

conditions and observation scheduling [6]. Furthermore, the limited resources of precision telescopes compared to the vast amount of space debris further restrict the acquisition of high-quality data. Short-segment data often fails to cover the complete attitude cycle; for example, when the observation length is less than a complete cycle, periodic analysis-based methods are difficult to apply effectively. In addition, observation noise sources are complex, including atmospheric disturbances, instrument errors, and background light pollution. High noise not only masks true attitude information but may also introduce spurious features. These factors collectively increase the uncertainty and complexity of attitude inversion.

Data-driven photometric curve analysis methods [7] have gradually become a research hotspot. Related research attempts to use deep neural networks to model photometric curves for target classification or parameter estimation. However, relying solely on deep learning methods often lacks explicit characterization of local structural features and has limited generalization ability under small sample or complex dynamic conditions. Meanwhile, existing research mainly focuses on parameter estimation, lacking systematic modeling and representation of the "attitude fingerprint information" of space debris [8]. In this work, we propose Photometric Light Curve Attitude Fingerprint Network (PAFNet) for analyzing the attitude fingerprint information of space debris based on light curves. Three contributions of PAFNet are listed as follows.

(1) Photometric simulation model of space debris integrating geometric structure and reflection characteristics is constructed to generate light curve data with controllable parameters based on physical mechanisms.

(2) The feature extraction for light curves integrating Shapelets and neural networks is contrived to achieve joint representation of local temporal patterns and global nonlinear features.

(3) The attitude inversion based on photometric information is established, realizing the extraction and analysis of space debris attitude fingerprint information.

2. Related Works

2.1. Photometric simulation models

In 2013, Cognion[9] proposed a model to describe the reflected light from the main components of space debris. This model can explain the significant increase in observed brightness of some space debris when the phase angle is greater than 100°. The model approximates space debris as a

Lambertian sphere and represents its photometric characteristics as the superposition of four contributions: diffuse reflection of sunlight from the debris itself (Lambertian sphere), reflection of sunlight from the front (light-receiving surface) of the solar panel (flat panel model), reflection of Earth's albedo from the debris itself, and reflection of Earth's albedo from the back of the solar panel. Comparison with existing empirical models and actual observation data shows that this model has good consistency, not only enabling independent analysis of each reflected flux component but also providing important evidence for understanding the physical source of space debris photometric signals. However, this model only considers the diffuse reflection effect and does not introduce specular reflection mechanisms. Therefore, for space debris with significant specular reflection characteristics, its simulation accuracy will decrease significantly, limiting the applicability of the model to complex objects.

In 2014, Bradley and Axelrad [10] evaluated the feasibility of a shape inversion method based on light curves by analyzing simulated photometric data acquired by space-based sensors in sun-synchronous orbit. The research subjects included upper-stage rocket bodies, high surface-to-mass objects, cubic fragments, and box-wing structure fragments. Their light curve simulation employed a reflection model combining the Lommel–Seeliger law and Lambert's law, a combination that effectively simulates the photometric variation characteristics of asteroids and exoplanets. In 2020, Kelecy et al.[11] modeled the photometric observation process of ground-based optical telescopes using the Cook–Torrance reflection model. This method expresses the observed photometric as a function of multiple factors, including fragment physical properties, spatial location, observation site, and solar irradiance conditions, thus providing a more comprehensive description of the photometric variation mechanism. In the same year, Rush et al. [12] introduced the Ashikhmin–Shirley reflection model combined with ray tracing methods to simulate and analyze the photometric characteristics of cuboid, cylindrical, and box-wing structure space fragments. The results show that there are significant differences between the simulated data generated by the reflection model and the actual observation data. To match the simulation results with the actual observed amplitudes, the reflectivity parameters of each research target need to be significantly reduced, which also reflects that the applicability of the current reflection model in modeling real space debris still has certain limitations.

2.2. Data-Driven Analysis of Photometric Light Curves

Deep learning has been widely used in astronomy [13] and the analysis of light curves contain high value and are worth exploring [14]. The classification problem of light curves [15] can be transformed into a time series classification problem [16], which is an important and challenging problem in data mining and a general task that has been applied in many fields. Time series data is a sequence with sequential attributes, which can be subdivided into single-index time series classification and multi-index time series classification. Light curves mainly reflect the change of brightness over time and belong to single-index time series. Therefore, the discussion focuses on the single-index time series classification problem. Time series classification can assist in matching algorithms with data, selecting algorithms, improving accuracy, and reducing computation in the fields of time series data prediction and anomaly detection. The Shapelets classification algorithm [17] classifies by finding the most discriminative subsequence in the sequence, where Shapelets refers to a best-matching subsequence that is independent of position. This type of algorithm is suitable for classification problems where a class can be defined by a pattern in the sequence, but the position of the pattern is irrelevant. The Shapelets algorithm has a certain degree of interpretability, but it is highly complex. There are also some studies on improving its performance [18] and pruning [19]. Because the Shapelets classification algorithm requires a lot of time to search for subsequences, it is more suitable for short sequences.

Based on the unique effects and characteristics of different physical processes in light curves, variable objects are classified including detection of candidate objects and astronomical phenomena, and classification of object types and variable stars [20]. The inherent challenges in light curve classification need to be addressed, including finding features that distinguish objects, and proposing robust feature extraction methods and light curve classification methods [21]. Research on the construction of training sets for light curve classification is essential. Xu et al. [22] used time-domain data from ZTF and non-variable source data from SDSS, and established a statistical model through cross-validation calculations to identify LAMOST variable sources, releasing a dataset of 631,769 LAMOST variable source candidates. Neira et al. [23] constructed a dataset consisting of light curves of 4,869 transient objects and 71,207 non-transient objects based on data released by the Catarina Real-Time Transient Observation Project (CRTS), and tested the dataset using binary

and octal classification tasks. Tsang et al. [24] developed a classifier for periodic light curves based on a recurrent neural network (RNN) autoencoder. Mcwhirter et al. [25] focused on processing non-uniform time series through representation learning of useful features using principal component analysis.

Currently, there is still a gap between light curve data and artificial intelligence techniques. To prepare the data and match it, we need to combine light curve data with existing deep learning frameworks. Since the training set for light curve classification is relatively small, and the quality of the training set directly affects the research on light curve classification techniques and methods, we need to propose a method for constructing a light curve training set. We can combine the traditional local feature class method Shapelets and the feature selection method [26] to form feature engineering in the construction method of light curve training set. Based on the extracted light curve features, we can study the light curve classification method, improve the effect of light curve classification, and explore its interpretability.

2.3. Target Characteristic Inversion Based on Photometry

The study of the characteristics of space debris based on photometric data is a complex and important topic. Research in this field mainly focuses on two aspects, geometric shape inversion and attitude inversion [27]. These two aspects are interconnected and together constitute the interpretation of the characteristics of space debris. Regarding geometric shape inversion, current methods for inverting the shape of artificial celestial bodies can be divided into three main categories, Extended Gaussian Image (EGI), statistical estimation methods, and deep learning methods [28]. EGI, as a tool for describing and reconstructing the geometry of objects, plays a crucial role in space debris research. In 2022, Robinson et al. [29] introduced a vertex displacement method that leverages the EGI closure error vector during EGI optimization to address concave reconstruction problems. This approach performs effectively in certain scenarios. For instance, when the concave boundary lies on a single plane, such as in the case of a rocket nozzle, the method can accurately reconstruct the concave geometry. However, its performance degrades in more complex configurations where concave boundaries span multiple planes, such as in box-wing satellite structures. In these cases, bilateral or mirror symmetry in the observed shadows causes the contributions from individual shadow sources to overlap or become indistinguishable. As a result,

the EGI closure error no longer provides sufficient information to uniquely resolve each contributing surface, making accurate shape reconstruction challenging.

In addition to the EGI-based methods, statistical estimation approaches also play an important role in acquiring target shape information. These methods primarily utilize statistical models, Bayesian inference, and filtering algorithms to fuse multi-source data, thereby achieving more accurate shape estimation. Commonly used statistical estimation techniques include the Extended Kalman Filter (EKF) [30], the Unscented Kalman Filter (UKF) [12], and the Particle Filter (PF) [31]. Howard et al. [32] employed simulated light curves to train various machine learning models and found that the Random Forest algorithm achieved the best performance in target shape and stability classification. However, this study has several limitations. For example, it did not explore more advanced approaches, and the shape classification task was combined with stability classification, as also discussed in the work of Linares et al. [33], which may have affected the overall accuracy of the results. To address these limitations, subsequent studies have adopted more advanced deep convolutional neural networks, conducting both simulation-based and experimental analyses to better interpret the light curves of space objects [34], [35].

3. Methods

3.1. Photometric Simulation Model

The luminosity of space debris is sum of radiant energy received per unit time from optical observation equipment, consisting of sunlight reflected from the debris, background light, and light scattered by the Earth. Among this, sunlight reflected from the space debris constitutes the majority, while other reflected light accounts for a smaller proportion and can be temporarily ignored in the analysis. The luminosity model of space debris is a coupling function of its shape, size, position, motion attitude, and surface material. Therefore, during the simulation, all of these influencing factors need to be considered to improve reliability, thereby enhancing the precision of future data analysis. The space debris simulation model described in this paper comprehensively considers relevant influencing factors and is implemented using the Python program. The flowchart is shown in Figure 1.

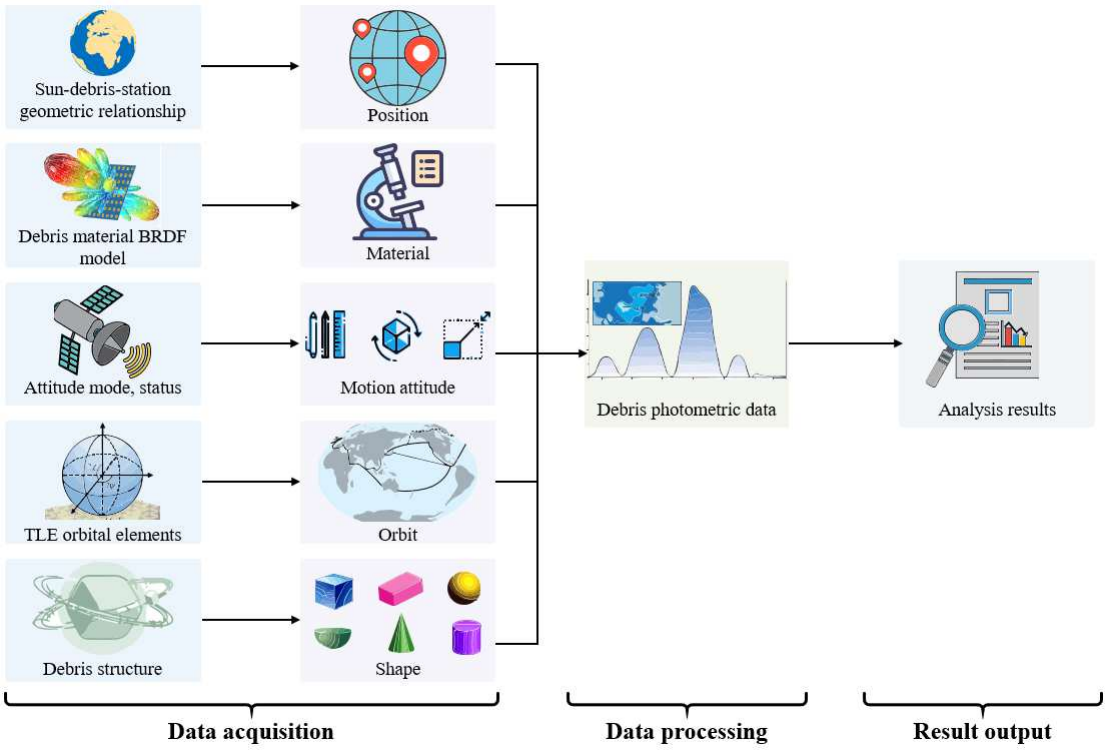


Figure 1. Schematic diagram of space debris photometric simulation process.

The shapes of space debris vary significantly, which are mainly determined by factors such as their size, payload, power supply system, and attitude control system. Due to their diverse origins and functions, space debris exhibits a wide range of geometric forms, including spherical, cylindrical, and cubic shapes. Let u_n, u_{t1}, and u_{t2} denote three orthonormal unit vectors defined in the body-fixed coordinate system. Among them, u_n is the surface normal vector, perpendicular to the illuminated side of the facet, while u_{t1} and u_{t2} lie within the facet plane and, together with u_n, form a right-handed coordinate system. Let s denote the unit vector pointing from the debris toward the Sun, and v denote the unit vector pointing from the debris toward the observation station. The unit vector h represents the bisector of the angle between s and v. The area of each facet is denoted by A. Superscript S denotes vectors expressed in the body-fixed coordinate system, while superscript J denotes vectors expressed in the inertial coordinate system. Space debris is generally assumed to be a rigid body. Therefore, the facet vectors remain constant during its motion.

When analyzing the illumination geometry of each facet, it is necessary to transform vectors to the inertial coordinate system. This transformation can be expressed as Equation 1.

$$u_i^B = A(q_I^B)u_i^I, \qquad i = u, v, n \tag{1}$$

where $A(q_I^B)$ is expressed in the form of a quaternion.

Space debris orbits under the influence of Earth's gravity. In the geocentric equatorial coordinate system, its equation of motion is expressed as Equation 2.

$$\ddot{r}^I = -\frac{\mu}{\|r^I\|^3} r^I + a_{pert}^I \tag{2}$$

where $\mu = 3.986 \times 10^{14}\ \mathrm{m}^3/\mathrm{s}^2$ denotes the Earth's gravitational parameter, and $\Delta \mathrm{v}$ represents the perturbation velocity caused by various forces.

A space object is subjected to Newton's laws of motion and the law of universal gravitation. When moving along a Keplerian orbit, only six orbital elements are required to uniquely determine its trajectory, namely the orbital inclination (i), the right ascension of the ascending node (Ω), the eccentricity (e), the argument of perigee (ω), the semi-major axis (a), and the mean anomaly (M_0). These six parameters are collectively referred to as the Keplerian orbital elements.

In this study, the positions of space debris are described using the analytical model based on TLE (Two-Line Element) orbital elements.

Let the position vector of the observation station in the geocentric equatorial coordinate system be $\mathrm{r}_{\mathrm{obs}}$, and the position vector of the space debris in the same coordinate system be r. Then, the position vector of the debris relative to the observation station is given by Equation 3.

$$d = r - R \tag{3}$$

The attitude of the space debris is represented using quaternions, which are based on the Euler axis/angle parameterization. For a given Euler axis e and rotation angle θ, the corresponding quaternion representation is given by Equation 4.

$$q = [q_1 \quad q_2 \quad q_3 \quad q_4]^T = \left[e_1 \sin\frac{\Phi}{2} \quad e_2 \sin\frac{\Phi}{2} \quad e_3 \sin\frac{\Phi}{2} \quad \cos\frac{\Phi}{2}\right]^T \tag{4}$$

These four quaternion components are not independent, and they satisfy the following normalization constraint in Equation 5.

$$q_1^2 + q_2^2 + q_3^2 + q_4^2 = 1 \tag{5}$$

The formula for representing the attitude matrix using quaternions is given by Equation 6.

$$A(q) = \begin{bmatrix} q_1^2 - q_2^2 - q_3^2 + q_4^2 & 2(q_1q_2 + q_3q_4) & 2(q_1q_3 - q_2q_4) \\ 2(q_1q_2 - q_3q_4) & -q_1^2 + q_2^2 - q_3^2 + q_4^2 & 2(q_2q_3 + q_1q_4) \\ 2(q_1q_2 + q_3q_4) & 2(q_2q_3 - q_1q_4) & -q_1^2 - q_2^2 + q_3^2 + q_4^2 \end{bmatrix} \quad (6)$$

The BRDF (Bidirectional Reflectance Distribution Function) is mathematically expressed to describe the radiance reflected in a given direction (θ_r, ϕ_r) relative to the irradiance incident on the debris surface from direction (θ_i, ϕ_i). The geometric diagram of BRDF is shown in Figure 2. Specifically, the BRDF is defined as the ratio of the reflected radiance to the incident irradiance, and can be written as Equation 7.

$$f(\theta_i, \varphi_i, \theta_r, \varphi_r) = \frac{dL(\theta_i + \varphi_i, \theta_r, \varphi_r)}{dE(\theta_i, \varphi_i)} \quad (7)$$

where $L_r(\theta_r, \phi_r)$ denotes the reflected radiance in the direction (θ_r, ϕ_r), and $E_i(\theta_i, \phi_i)$is the irradiance incident on the debris surface from direction (θ_i, ϕ_i).

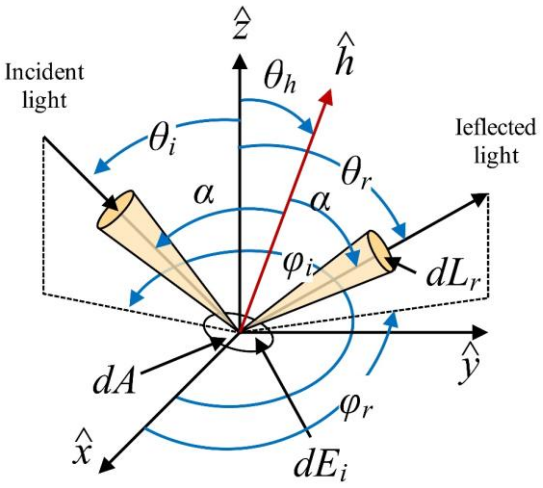


Figure 2. Geometric diagram of bidirectional reflection distribution function.

As illustrated in Figure 2, the bidirectional reflectance distribution function (BRDF) is a function of the incident angles (θ_i, ϕ_i), the reflection angles (θ_r, ϕ_r), and the wavelength (λ). This model decomposes the BRDF into two components, the specular reflection component and the diffuse reflection component, as shown in Equation 8-Equation 12.

$$\rho_{total} = \rho_{spec} + \rho_{diff} \quad (8)$$

$$\rho_{spec} = \frac{\sqrt{(n_u+1)(n_v+1)}}{8\pi} \frac{(u_n^I \cdot u_h^I)^z}{(u_h^I \cdot u_{sun}^I) max(u_n^I \cdot u_{sun}^I, u_n^I \cdot u_{obs}^I)} F_{reflect} \tag{9}$$

$$z = \frac{n_u (u_h^I \cdot u_u^I)^2 + n_v (u_h^I \cdot u_v^I)^2}{1 - (u_h^I \cdot u_n^I)^2} \tag{10}$$

$$F_{reflect} = R_s + (1 - R_s)(1 - u_{sun}^I \cdot u_h^I)^5 \tag{11}$$

$$\rho_{diff} = \frac{28 R_d}{23\pi}(1 - R_s)\left[1 - \left(1 - \frac{u_n^I \cdot u_{sun}^I}{2}\right)^5\right]\left[1 - \left(1 - \frac{u_n^I \cdot u_{obs}^I}{2}\right)^5\right] \tag{12}$$

where n_u and n_v are model parameters. The coefficients R_s and R_d represent specular reflection coefficient and diffuse reflection coefficient, respectively, of the debris surface, while $F_{reflect}$ denotes the Fresnel reflection function.

The solar irradiance incident on the debris surface is given by Equation 13.

$$F_{sun} = C_{sun} \rho_{total} u_n^I \cdot u_{sun}^I \tag{13}$$

where $E_{\text{sun}} = 455\ W/m^2$ is the visible solar irradiance per square meter incident on the debris surface. If no sunlight is reflected from the debris toward the observation station—that is, if the angle between the facet normal and the line of sight to the station, or between the facet normal and the incident solar direction, exceeds a threshold angle $\theta_{\max}$—then the reflected radiance $L_r = 0$ or the corresponding specular/diffuse contributions are set to zero.

The energy of sunlight observed at the station can be expressed as Equation 14.

$$F_{obs} = \frac{F_{sun} A_j u_n^I \cdot u_{obs}^I}{\|r_{obs}\|^2} \tag{14}$$

where r_c is the position vector of the debris relative to the observation station, and A_f is the area of a single facet on the debris surface.

The reflected solar energy can be further used to compute the apparent magnitude of the debris, given by Equation 15.

$$m_{app} = -26.7 - 2.5 \log_{10} \left| \frac{F_{obs}}{C_{sun}} \right| \quad (15)$$

where -26.7 is the apparent magnitude of the Sun.

In general, solar panels are composed of multiple material layers, typically two: the outer layer, often crystalline silicon, generates a photoelectric effect, while the inner layer, typically aluminum, provides high thermal conductivity. The main body of a debris object differs in material composition from solar panels. To minimize the effect of thermal radiation, the body surface is usually covered with multilayer insulation (MLI, Multilayer Insulation), composed of high-temperature resistant materials, such as polyimide films.

3.2. Light Curve Feature Extraction Using Shapelets and Neural Networks

In astronomical observations, different observation bands correspond to different observational attributes, and the light curves of each band exhibit different patterns and characteristics. Therefore, efficiently extracting effective information from the feature space of light curves is a core challenge in time-domain astronomy research. The analysis of space debris light curves also faces problems such as imbalanced multi-class samples and significant noise interference. To address this, the Shapelets method can be adopted. By extracting global Shapelets features that distinguish all debris, and combining them with Shapelets features specific to certain classes and samples, the representational ability of light curves and the effectiveness of attitude fingerprint extraction can be improved.

The feature engineering structure based on Shapelets is shown in Figure 3. This method can extract three types of Shapelets features as global class-distinguishing features, specific class-distinguishing features, and sample-specific features, which are used for subsequent classification, attitude analysis, and fingerprint information identification of debris light curves. Furthermore, since different debris exhibit local differences in rotation state and surface characteristics, the local light curve patterns extracted by Shapelets feature engineering also have a certain degree of interpretability, providing a theoretical basis and methodological support for attitude fingerprint analysis of space debris.

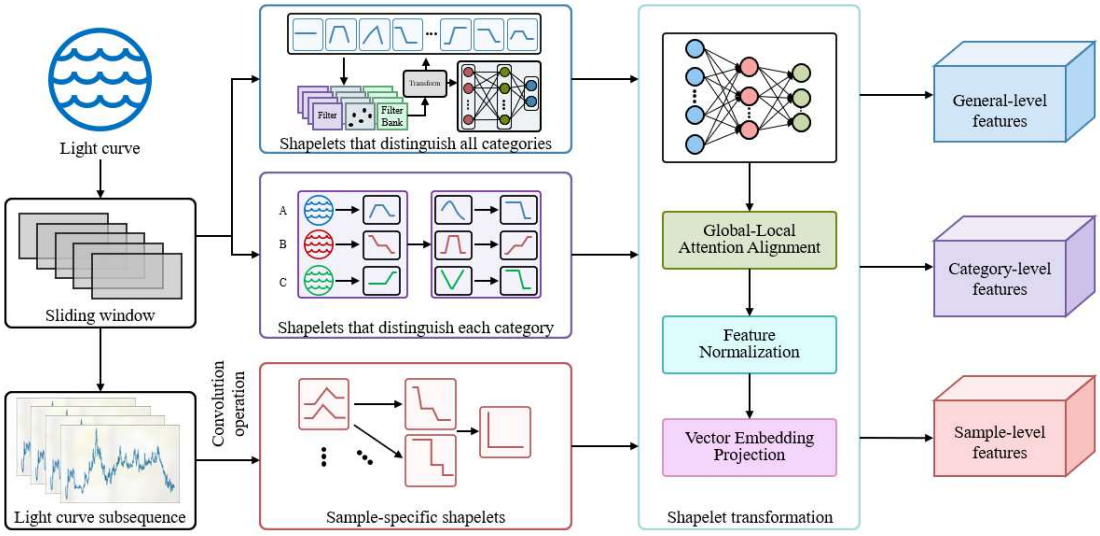


Figure 3. Structure of Shapelets-based feature engineering for light curve analysis.

Given a time series $T = t_1, t_2, \ldots, t_n$, a subsequence S consists of l consecutive values from T. A set of k is denoted as $Z = \{S_1, S_2, \ldots, S_k\}$. The distance between the i-th time series T_i and the j-th Shapelet S_j is defined as the minimum distance between S_j and every subsequence of T_i. A subsequence of length l starting at time step p in T_i is given by Equation 16.

$$T_{i,p:p+l-1} = t_{i,p}, t_{i,p+1}, \cdots, t_{i,p:p+l-1}{}^{T}, T_{i,p:p+l-1} \in R^{l\times 1} \tag{16}$$

The distance between the i-th time series T_i and the j-th Shapelet S_j is calculated as Equation 17.

$$h_{i,j} = \min_{p=1,2,\cdots,P} \sqrt{\sum_{w=1}^{l} t_{i,p+w-1} - S_{j,w}{}^{2}} \tag{17}$$

where $S_{j,w}$ represents the w-th value of Shapelet S_j, and $h_{i,j}$ denotes the Euclidean distance between T_i and Shapelet S_j.

This type of feature, similar to conventional Shapelet-based methods, primarily focuses on distinguishing all classes but often ignores minority classes or hard-to-classify classes in imbalanced datasets, which can affect the final classification performance. Therefore, this paper proposes two additional types of Shapelet features to compensate for this loss.

Shapelets for specific samples are used to extract particular features from light curves, which helps improve the flexibility of classification models. To obtain Shapelet features for specific

samples, a neural network–based Shapelet generator is designed. Sub-sequences of the input light curves (astronomical time series) are extracted using a sliding window, and then a convolutional layer is applied to generate Shapelet features.

The sliding window length is set to l with a step size of 1. For an astronomical time series of length n, $T_i = t_1, t_2, \dots, t_n$, this produces $p = n - l + 1$subsequences. All subsequences of $T_i$are concatenated together and denoted as C_i, as shown in Equation 18.

$$C_i = T_{i,1:l} \oplus T_{i,2:l+1} \oplus \cdots \oplus T_{i,n-l+1:n} \tag{18}$$

where $\oplus$ denotes concatenation, and $C_i \in \mathbb{R}^{l \times p}$.

Next, a convolution operation is performed along the time axis on C_i using a kernel of size $w \times p$with a stride of 1. $S_{i,j}^{c} \in \mathbb{R}^{l \times 1}$ denotes the j-th Shapelet generated from the astronomical time series T_i, as shown in Equation 19.

$$S_{i,j}^{c} = w_j * C_i + b_j \tag{19}$$

where $w_j \in \mathbb{R}^{w \times p}$ is the j-th filter of width w, b_j is the bias term, and $*$denotes the convolution operation. Using this method, k specific sample Shapelets are generated, and the Shapelet transformation Equation (Equation 17) is applied to extract the features of the specific sample.

Shapelets for a specific class are used to distinguish the light curves of that particular class from those of other classes. To ensure that the learned Shapelet features are associated with a specific class, an auxiliary binary classifier is employed. The input light curve data is transformed using the Shapelets of the specific class, and the resulting features are combined using a weighted sum. To simplify hyperparameter optimization, if there are mShapelets used to distinguish all classes, then $k = m/N_c$ Shapelets are used for distinguishing each individual class, where $N_c$denotes the total number of classes. For class c, set of Shapelets used to distinguish it is $S_c = \{s_1^c, s_2^c, \dots, s_k^c\}$.

Through feature engineering of light curves based on Shapelets, three levels of features were obtained. This chapter proposes an end-to-end discriminative model (MS-FCN) for classifying light curves, with the specific results shown in Figure 4. By training the classification model using a fully convolutional network, the probability distribution for each class is calculated. A binary classifier is then used to learn the class-specific features for each category, which helps to refine the final results.

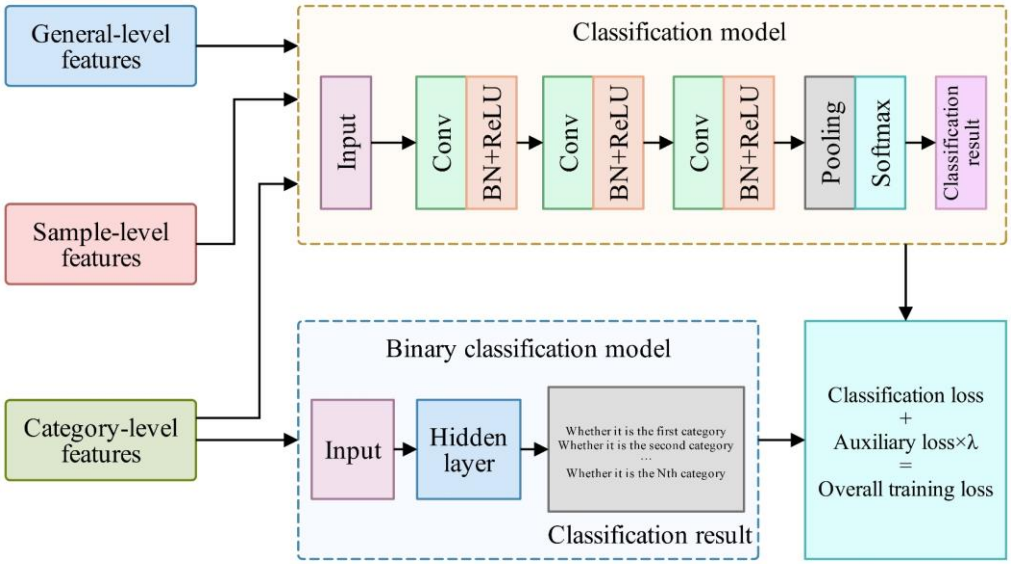


Figure 4. End-to-end discrimination model diagram for feature engineering of light curves based on Shapelets.

After transforming the features from the three types of Shapelets, these features are combined into a single vector, as described in Equation 20.

$$H_i = h_j \oplus h_i^c \oplus h_i^s \tag{20}$$

where h_i, h_i^c, and h_i^s represent the general-level features, class-level features, and sample-level features, respectively.

Figure 4 also shows the specific design of the auxiliary binary classifier. The left unit represents the Shapelet-transformed features for each specific class, the middle unit computes their weighted sum, and the sigmoid activation function is then applied. By performing the Shapelet transformation on a time series T_i using Equation 17, a new representation h_i^c is obtained as input to the auxiliary binary classifier, as Equation 21.

$$Pc|T_i = sigmoid f_{c,i},\ f_{c,i} = w_c h_{c,i} \tag{21}$$

where w_c represents the weights of the auxiliary binary classifier, and $P_{c|T_i}$ denotes the probability that the light curve sample T_i belongs to class c.

3.3. Photometry-Based Attitude Determination

Attitude inversion can improve the reliability and accuracy of target attitude determination under short-arc light conditions while reducing the requirements for the amount of photometric data and feature complexity. It provides an effective method for extracting debris attitude information from limited or noisy light curve observations.

Assume that the target rotates around its center of mass in the $o_T T'Z'$coordinate system, with an angular velocity ω. Then, the motion of $f_f l$can be decomposed into three components. Assume that the angular velocity ω in the body-fixed coordinate system $o_j ryz^*$has projections along the $o_j t$, r^*, and z^*axes denoted by p, q, and r, respectively. Then, the instantaneous angular velocity of the target in the $o_T T'Z'$coordinate system can be expressed in terms of the Euler angles and their derivatives as Equation 22.

$$\begin{cases} p = \dot{\psi}\sin\theta\sin\varphi + \dot{\theta}\cos\varphi \\ q = \dot{\psi}\sin\theta\cos\varphi - \dot{\theta}\sin\varphi \\ r = \dot{\psi}\cos\theta + \dot{\varphi} \end{cases} \tag{22}$$

From Equation 22, the rate of change of the Euler angles can be expressed as Equation 23.

$$\begin{cases} \dot{\psi} = \dfrac{1}{\sin\theta}(p\sin\varphi + q\cos\varphi) \\ \dot{\theta} = p\cos\varphi - q\sin\varphi \\ \dot{\varphi} = r - \dot{\psi}\cos\theta \end{cases} \tag{23}$$

For space debris over a short orbital arc, because the arc segment is short, the effects of gravity gradient torque, atmospheric drag torque, and other perturbations can be neglected. Therefore, the angular momentum $\mathbf{H}$ of the target rotating about a fixed point satisfies, in the body-fixed coordinate system, that the moments of inertia $J_x, J_y, J_z, J_{xy}, J_{yz}, J_{xz}$ are constant, as shown in Equation 24.

$$\frac{dH}{dt} = 0 \tag{24}$$

To eliminate the centrifugal products of inertia J_{xy}, J_{yz}, J_{xz}, the principal axes of inertia at the fixed point are chosen as the body axes. Then the angular momentum can be simplified as Equation 25 and Equation 26.

$$H = I_x\omega_x i + I_y\omega_y j + I_z\omega_z k \tag{25}$$

$$H_x = I_x\omega_x, H_y = I_y\omega_y, H_z = I_z\omega_z \tag{26}$$

In the body-fixed coordinate system $Ox^*y^*z^*$, the axes rotate together with the rigid body. Therefore, the angular velocity of the coordinate system equals the angular velocity of the rigid body. Replacing the absolute derivative in Equation 24 with the relative derivative. Let $A = I_x, B = I_y, C = I_z$, then Equation 24 expands to the classical Euler equations for a rigid body rotating about a fixed point, as shown in Equation 27.

$$\begin{cases} A\dot{p} + (C - B)qr = 0 \\ B\dot{q} + (A - C)rp = 0 \\ C\dot{r} + (B - A)pq = 0 \end{cases} \tag{27}$$

This is called Euler's case of rigid body motion about a fixed point.

$$H_x = Ap, H_y = Bq, H_z = Cr. \tag{28}$$

Specifically, in Euler's case, if two of the principal moments of inertia about point O are equal, e.g., $A = B$, the rigid body is dynamically symmetric, and the z^*-axis is the axis of dynamic symmetry. In this situation, the angular momentum is constant. Its components along the body axes can be expressed as Equation 29.

$$\begin{cases} H_x = Ap = H\sin\theta\sin\varphi \\ H_y = Aq = H\sin\theta\cos\varphi \\ H_z = Cr = H\cos\theta \end{cases} \tag{29}$$

Substituting Equation 29 into the third equation of Equation 27 gives Equation 30.

$$r \equiv r_0 = const. \tag{30}$$

Equation 30 indicates that the projection of the angular velocity along the dynamically symmetric axis is constant. Substituting into Equation 29, the polar angle θ_0 between the dynamic symmetry axis and the angular momentum vector is constant, as shown in Equation 31.

$$\theta \equiv arccos\left(\frac{Cr_0}{H}\right) \equiv \theta_0 = const. \tag{31}$$

Then, combining Equation 30 and Equation 31 with Equation 22 yields Equation 32 and Equation 33.

$$\begin{cases} p = \dot{\psi}\sin\theta_0\sin\varphi \\ q = \dot{\psi}\sin\theta_0\cos\varphi \\ r_0 = \dot{\psi}\cos\theta_0 + \dot{\varphi} \end{cases} \tag{32}$$

$$\begin{cases} \dot{\psi} = \dfrac{H}{A} \equiv \omega_2 = const \\ \dot{\varphi} = r_0 - \dfrac{H}{A}\cos\theta_0 = \dfrac{A-C}{A} \\ r_0 \equiv \omega_1 = const \end{cases} \tag{33}$$

The orientation parameters of the target in space include $(\alpha, \beta, \gamma, e, i, \Omega, \ldots)$. For a specific observation arc, these can be calculated from the observation time, station position, orbital elements, and phase angle. Considering the principal moments of inertia approximately as $I_x : I_y : I_z = 4:4:3$, the following relations hold as shown in Equation 34.

$$\begin{cases} Cr = H\cos\theta_H \\ \theta_H = \theta_{H0} \\ \dot{\psi}_H \equiv \dfrac{H}{A} \equiv Cr_0/(A\cos\theta_{H0}) \\ \dot{\varphi}_H \equiv \dfrac{(A-C)r_0}{A} \\ \psi_H = \psi_{H0} + \dot{\psi}_H t \\ \varphi_H = \varphi_{H0} + \dot{\varphi}_H t \end{cases} \tag{34}$$

This indicates that by introducing just a few additional parameters, the corresponding time series of orientation angles can be uniquely determined. The inversion process searches, under the constraints of attitude angle variation, for the light curve in the database that best matches the measured light curve using a genetic algorithm. A special case exists when $\phi = 0$or $180°$, which can produce equivalent solutions. To eliminate such degenerate solutions, $\phi$is constrained within $0°$to $90°$. We use a genetic algorithm to search for the attitude parameters corresponding to the observed light curve. Let P_s denote the observed brightness and P_f denote the brightness in the light curve database. The fitness function for the genetic algorithm is designed as Equation 35.

$$\begin{cases} Fitness = \dfrac{1}{2}\left(\dfrac{\dfrac{1}{P_1}}{\dfrac{\sum_{k=1}^{N}\dfrac{1}{(P_2)^2+0.01}}{\sum_{k=1}^{N}(P_1)}} + \dfrac{1}{0.01 + 0.01\left(\sum_{k=1}^{N}\dfrac{|P_2|}{N}\right)} \right) \\ P_1 = P_{s_k} - min(Ps) \\ P_2 = P_{sn_k} - P_{in_k} \end{cases} \tag{35}$$

where P_i' represents a normalized version of P_s. The maximum value of this fitness function is 100, which indicates that P_s and P_f differ only by a translation; in other words, the magnitude and trend of brightness variation are completely consistent.

4. Experiments

4.1. Datasets and Setup

The variation of photometric signals of space debris is primarily influenced by changes in the instantaneous rotational state and the corresponding variation in surface light scattering properties. In the simulation, these factors are considered when setting specific parameters and experimental conditions. Based on the typical structure and scale of space debris, the simulated target is modeled as a rectangular cuboid with unequal edge lengths of 0.7 m, 0.4 m, and 0.2 m. Considering the trade-off between facet discretization resolution and computational efficiency, the facet size is set to 0.1 m. The target surface material is chosen as a representative debris material with facet dimensions of 0.03 m × 0.03 m × 0.01 m. The experimental setup includes a rotational motion platform and a Daheng MER-131-210U3M detector, with parameters shown in Table 1. Attitude inversion can be performed on simulated light curves with varying noise levels. Specifically, for each light curve, 600 iterations are first conducted to obtain a preliminary parameter range, followed by 200 iterations on a secondary grid to refine the attitude parameters.

The simulated dataset is constructed by incorporating object geometry, orbital configuration, and surface reflection properties, allowing controlled variation of attitude parameters and noise levels. This enables systematic evaluation of the proposed method under different observational conditions. To reduce potential bias introduced by fully simulated data, the feature extraction approach is additionally evaluated on publicly available astronomical light curve datasets, such as those from the Zwicky Transient Facility [36]. Although these datasets do not correspond to space debris, they provide real observational time-series data with varying noise and sampling characteristics, which are useful for assessing the generalization ability of the feature representation.

Table 1. Experimental setup parameters.

Category	Parameter	Value / Description
Detector System	Focal length	500 m
	Pixel size	15 μm

	Target–detector distance	2 m
	Source–detector angle	10°
Motion Setup	Platform	Rotating turntable
	Target position	Fixed at center of turntable
	Rotation axis	Adjustable via turntable azimuth
	Angular velocity	Constant
	Observation	Full rotation cycle recorded

4.2. Attitude Inversion Algorithm Analysis

To further improve accuracy, a secondary grid is applied within this constrained range, and a genetic algorithm is used to refine the attitude parameters. Table 2 indicates that, for photometry with 0.5 magnitude noise (N), the initial solution range is relatively wide due to a lower fitness threshold for initial selection.

Table 2. Preliminary range of observation noise (N) and final inversion results of direct inversion.

Parameters	Parameter range		Final result	
	0	0.5	0	0.5
$r_0(°/s)$	2.6666±0.001	2.6688±0.0196	2.6400	2.6290
$\xi_0(°)$	29.68±7.44	34.59±8.98	29.72	28.66
$\eta_0(°)$	40.96±3.78	33.99±12.59	39.58	39.44
$\psi_{H0}(°)$	22.90±5.55	5.84±83.40	19.78	23.48
$\theta_{H0}(°)$	59.41±3.90	57.44±9.90	59.43	54.83

To evaluate the noise resistance of PAFNet, this work performs direct inversion of photometric data under different noise levels. Specifically, using the inversion method described in the previous section, the observation noise gradually increased from magnitude 0.0 to magnitude 1.0, and the corresponding light curves are used for attitude inversion. Considering that observation noise can affect fitness assessment, to compare the inversion results under different noise conditions, we calculate the fitness of the photometric values corresponding to the inverted attitude parameters relative to the denoised observation photometric values, which are listed in Table 3. Furthermore, the deviations between the inverted attitude parameters and the preset attitude values under different noise levels are listed in Table 4.

Table 3. Direct inversion results under different observation noise (N).

N	$r_0(°/s)$	$\xi_0(°)$	$\eta_0(°)$	$\psi_{H0}(°)$	$\theta_{H0}(°)$	Fitness
Preset Value	2.6400	29.70	39.60	19.80	59.40	99.00

0.0	2.6400	29.73	39.58	19.78	59.43	98.98
0.1	2.6400	30.83	39.95	18.50	58.99	97.55
0.2	2.6400	29.12	39.75	19.31	58.87	96.36
0.3	2.6399	33.49	42.75	17.47	57.74	84.24
0.4	2.6399	30.72	45.30	25.53	54.78	81.16
0.5	2.6290	28.66	39.44	23.48	54.83	76.42
0.6	2.6345	35.47	31.62	9.90	56.03	70.63
0.7	2.6346	25.77	41.52	21.28	55.07	81.08
0.8	2.6399	35.83	40.33	13.55	54.66	78.19
0.9	2.7204	27.22	33.60	9.90	53.80	66.47
1.0	2.7204	31.76	39.11	21.03	54.53	76.24

Table 4. The deviation between the direct inversion result and the true value.

N	$\lvert\Delta r_0\rvert(°/s)$	$\lvert\Delta\xi_0\rvert(°)$	$\lvert\Delta\eta_0\rvert(°)$	$\lvert\Delta\psi_{H0}\rvert(°)$	$\lvert\Delta\theta_{H0}\rvert(°)$
0.0	0.0000	0.03	0.02	0.02	0.03
0.1	0.0000	1.13	0.35	1.30	0.41
0.2	0.0000	0.58	0.15	0.50	0.53
0.3	0.0001	3.79	3.15	2.33	1.66
0.4	0.0001	1.02	5.70	5.73	4.62
0.5	0.0109	1.04	0.16	3.68	4.57
0.6	0.0055	5.77	7.98	9.90	3.37
0.7	0.0054	3.93	1.92	1.48	4.33
0.8	0.0001	6.13	0.73	6.25	4.74
0.9	0.0804	2.48	6.00	9.90	5.60
1.0	0.0054	2.06	0.49	1.23	4.87

The direct inversion results under varying observation noise N show that the angular velocity r_0 remains highly stable, with minimal deviation even at high noise levels, indicating strong robustness. In contrast, the Euler angles $\xi_0$and η_0 are more sensitive to noise, with deviations increasing noticeably as N rises, reaching up to 6.13° and 9.90° at higher noise levels. The initial heading angles ψ_{H0} and θ_{H0} also experience moderate deviations, particularly at $N = 0.6$,0.8, and 0.9, where errors approach 9.90° and 5–6°, reflecting the impact of observation noise on orientation estimation. Correspondingly, the fitness metric declines from near-perfect values of 98.98 at $N = 0.0$ to as low as 66.47 at $N = 0.9$, illustrating the overall deterioration in inversion accuracy as noise increases. Overall, PAFNet performs reliably under low noise, accurately recovering most parameters, while higher observation noise substantially degrades the accuracy of Euler and heading angles, highlighting the sensitivity of these parameters to measurement errors.

These results indicate that, for observed brightness variations of about 2.5 magnitudes, even with noise up to 1.0 magnitude, the inverted brightness closely matches the true brightness.

To evaluate the sensitivity of the fitness function to different attitude parameters, we varied the parameters around their values corresponding to the maximum fitness. The variation ranges were set to $(0.0020°/s, 10.00°, 10.00°, 10.00°, 10.00°)$, to observe how changes in the attitude parameters affect the fitness. The numerical changes in fitness are shown in Table 5. The fitness is more sensitive to changes in ψ_{H0} and θ_{H0} than to changes in α and η_0. Therefore, in cases where it is not possible to fully resolve all four angular parameters $(\xi_0, \eta_0, \psi_{H0}, \theta_{H0})$, particular attention should be paid to ψ_{H0} and θ_{H0}.

Table 5. Direct inversion and changes in fitness caused by variations in attitude parameters.

N	$r_0(0.0020°/s)$	$\xi_0(10.00°)$	$\eta_0(10.00°)$	$\psi_{H0}(10.00°)$	$\theta_{H0}(10.00°)$
0.0	35.93	4.54	11.86	2.56	25.01
0.1	24.78	0.98	2.70	0.43	11.96
0.2	16.34	0.36	1.20	0.22	6.25
0.3	12.60	0.19	0.31	0.10	3.73
0.4	8.50	0.20	0.40	0.06	2.45
0.5	6.58	0.08	0.19	0.12	1.90
0.6	5.49	0.01	0.16	0.13	2.23
0.7	4.03	0.09	0.23	0.03	1.33
0.8	3.63	0.06	0.19	0.04	1.65
0.9	2.77	0.11	0.13	0.05	0.91
1.0	2.59	0.06	0.07	0.02	0.73

In practical applications, during the photometric inversion of attitude parameters, observation noise, as part of the information, is included in the fitness calculation. Therefore, noise affects the selection of attitude parameters during the inversion. To reduce the impact of noise, we attempted to preprocess the photometric data by smoothing it before attitude calculation, eliminating some of the noise interference before calculating the attitude parameters. The noise introduced by photometry increased from 0.0 magnitude to 1.0 magnitude. The results of the inversion after smoothing are shown in Table 6. The maximum deviations of each attitude parameter are $|\Delta r_0|_{max} = 0.07587$ s, $|\Delta\xi_0|_{max} = 8.83°$, $|\Delta\eta_0|_{max} = 10.00°$, $|\Delta\psi_{H0}|_{max} = 10.00°$, $|\Delta\theta_{H0}|_{max} = 4.83°$. Compared with the case of direct inversion, the deviations of all attitude parameters are reduced after smoothing.

Table 6. Inversion attitude results after smoothing.

N	$r_0(°/s)$	$\xi_0(°)$	$\eta_0(°)$	$\psi_{H0}(°)$	$\theta_{H0}(°)$	Fitness
Preset Value	2.6400	29.70	39.60	19.80	59.40	—
0.0	2.6400	29.72	39.60	19.78	59.40	99.00
0.1	2.6400	29.54	39.94	18.96	59.53	97.89
0.2	2.6400	27.96	40.12	23.36	57.98	95.18
0.3	2.6400	29.12	39.99	19.70	58.03	92.58
0.4	2.6400	25.97	39.24	24.90	57.87	91.02
0.5	2.6400	30.01	40.95	22.50	56.71	89.51
0.6	2.6400	38.44	42.05	26.17	54.66	61.80
0.7	2.6455	34.74	46.02	9.90	55.71	79.93
0.8	2.6400	28.95	41.60	23.19	54.62	83.65
0.9	2.5650	32.65	49.50	29.70	56.10	75.48
1.0	2.5704	36.55	48.62	24.68	56.81	76.29

4.3. Ablation Studies

To evaluate the contribution of each component in PAFNet, a series of ablation experiments are conducted. The noise level is set to 0.5. Results of ablation experiments are shown in Table 7.

Table 7. Results of ablation experiments.

Model	Shapelets	Neural Network	Single Light Curve	Multiple Light Curve	Fitness
PSM-multi	×	×	×	✓	70.44
PSM-Sh-multi	✓	×	×	✓	79.21
PSM-NN-multi	×	✓	×	✓	75.42
Single-Curve	✓	✓	✓	×	61.24
PAFNet	✓	✓	×	✓	**89.51**

First, the baseline model PSM-multi, which relies purely on the photometric simulation model without any learned feature extraction, shows the lowest performance among the multi-curve approaches. This indicates that physical modeling alone is insufficient to capture the complex nonlinear patterns in photometric light curves, especially under noise conditions. When Shapelets are introduced, performance of PSM-Sh-multi improves significantly from 70.44 to 79.21 in Fitness. This demonstrates that Shapelets effectively capture local temporal patterns in light curves, which are highly relevant for representing attitude-dependent brightness variations. Compared to the neural network-only model (PSM-NN-multi), Shapelets provide a larger improvement, suggesting that interpretable local features are more critical than purely global nonlinear mappings in this task. The PSM-NN-multi model still outperforms the baseline, confirming that neural networks can learn global nonlinear relationships in the data. The Single-Curve model shows a substantial drop in

performance despite using both Shapelets and neural networks. This highlights a key limitation as a single light curve does not provide enough information for stable and accurate attitude inversion.

Finally, the full PAFNet model achieves the best performance with Fitness of 89.51, significantly outperforming all ablated variants.

4.4. Fitness Impact Analysis

This section investigates the effect of noise levels and observation conditions on the inversion results. It examines how the initial parameter range, fitness thresholds, and multi-arc combination influence the final attitude estimation accuracy, thereby validating the reliability and adaptability of PAFNet.

The essence of inverting a target's attitude from light curves is to search the database for brightness curves that match the measured light curve. Therefore, the quality of the light curve itself constrains the accuracy of the inverted attitude parameters. To study the influence of a single light curve, we assume that only one light curve is available at a time. For each light curve, we perform 600 rounds of attitude calculations and then compute the deviation between the average of the 600 results and the true values, as well as the standard deviation of the 600 results. The results show that, for any single light curve, the calculated results not only exhibit a considerable deviation from the true values, but the 600 repeated calculations are also relatively dispersed. To improve inversion accuracy, we jointly invert three light curves. The statistical results are shown in Figure 5.

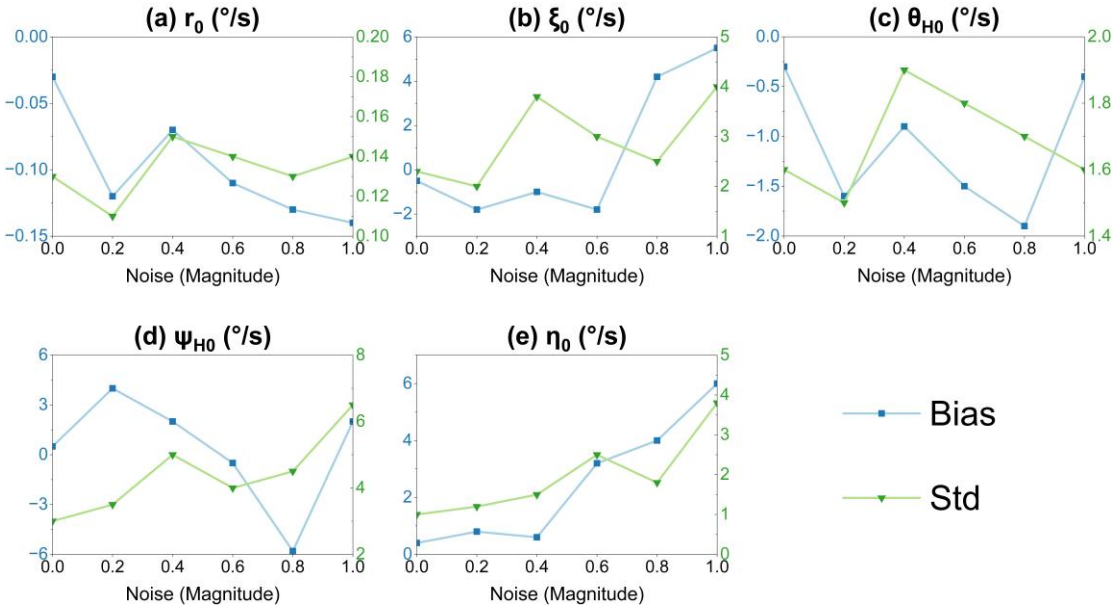


Figure 5. Statistical analysis of attitude parameters obtained by jointly solving three optical curves.

Both the deviations of the averaged parameters from the true values and the standard deviations of the results are effectively reduced. Specifically, the deviation of r_0 is within 0.15°/s. The deviation of ξ_0 and ψ_{H0} are both within 7°. The deviation of η_0 is within 10° and the deviation of θ_{H0} is within 2°. Under ideal conditions, by combining three light curves, the deviations of all angular parameters from the true values are less than 10°, and the deviation of r_0 is less than 0.15°/s.

These analyses demonstrate that associating multiple light curves can significantly improve the accuracy and precision of attitude inversion. In practice, observational data are limited by system noise, sky conditions, and other factors, so the measured brightness deviates from the ideal brightness. By comparing observed data with standard celestial calibrators, the observational precision of the equipment can be determined, allowing calibration of the system's stability and accuracy. It should be noted that the inversion process of measured brightness relies on the ideal brightness in the database. Therefore, the fitness decreases as observational precision decreases. On the other hand, for light curves with the same observational precision, differences in amplitude can also affect the fitness corresponding to the true attitude.

5. Conclusion

This paper addresses the problem of estimating attitude information of space debris from photometric light curves by proposing the Photometric Light Curve Attitude Fingerprint Network (PAFNet). The framework combines photometric modeling with data-driven feature analysis to extract attitude-related information from light curves. For attitude inversion, a genetic algorithm–based approach is used to identify the attitude parameters by matching observed light curves with a simulated database. Experimental results indicate that the proposed method can estimate attitude parameters with reasonable accuracy under different noise conditions, including cases with noise levels up to 1.0 magnitude. In addition, smoothing of photometric data helps reduce estimation errors, and combining multiple light curves improves the stability of the inversion results. The analysis also shows that different attitude parameters exhibit varying sensitivity to photometric variations, which may be useful for practical parameter estimation. Despite its effectiveness, the proposed method has several limitations. The experiments are mainly based on simulated data,

which may not fully reflect real observational conditions such as atmospheric effects and calibration errors. The inversion performance also depends on the accuracy of the photometric model, and mismatches in surface reflectivity may introduce errors. In addition, the use of a genetic algorithm leads to relatively high computational cost, limiting efficiency in large-scale applications. The estimation of some attitude parameters remains sensitive to high noise and short observation arcs, and the current model is limited to relatively simple object geometries. Future work will focus on validation with real observational data, improving reflection models, and enhancing computational efficiency through alternative or hybrid optimization methods. Extensions to more complex debris shapes and the integration of multi-source observations will also be investigated to improve robustness and reliability.

Data Availability

All data generated or analysed during this study are included in this published article and its supplementary information files. Public astronomical light curve data can be accessed through the official data release platforms of the Zwicky Transient Facility (https://github.com/ZwickyTransientFacility).

Funding Declaration: This research is supported by National Science and Technology Major Project(2022ZD0117301).

Reference

[1] S. Kaineg, "The growing problem of space debris," *Hastings Envt'l LJ*, vol. 26, p. 277, 2020.
[2] S. Afshar, A. P. Nicholson, A. Van Schaik, and G. Cohen, "Event-based object detection and tracking for space situational awareness," *IEEE Sensors Journal*, vol. 20, no. 24, pp. 15117–15132, 2020.
[3] J. Šilha, M. Zigo, T. Hrobár, P. Jevčák, and M. Verešvárska, "Light curves application to space debris characterization and classification," *Complexity*, vol. 10, p. 3, 2021.
[4] T. Schildknecht *et al.*, "Photometric monitoring of non-resolved space debris and databases of optical light curves," presented at the Advanced Maui Optical and Space Surveillance Technologies

Conference, 2015, p. 25.
[5] D. Hampf, P. Wagner, and W. Riede, “Optical technologies for the observation of low Earth orbit objects,” *arXiv preprint arXiv:1501.05736*, 2015.
[6] O. Olurope, U. Ukommi, and R. Udoh, “Comparative coverage and horizon plane analysis for leo, meo, geo and heo satellites,” *Journal of Multidisciplinary Engineering Science and Research (JMESR)*, vol. 1, no. 2, pp. 54–56, 2022.
[7] F. M. de Oliveira, M. V. dos Santos, and R. R. Reis, “Data-driven photometric redshift estimation from type Ia supernovae light curves,” *Monthly Notices of the Royal Astronomical Society*, vol. 518, no. 2, pp. 2385–2397, 2023.
[8] M. Kuhn, M. Michel, and T. Dekorsy, “PHOTOMETRIC COMPOSITE FINGERPRINTS FOR RESIDENT SPACE OBJECTS”.
[9] R. L. Cognion, “Observations and modeling of GEO satellites at large phase angles,” *AMOS proceedings*, 2013.
[10] B. K. Bradley and P. Axelrad, “Lightcurve inversion for shape estimation of geo objects from space-based sensors,” presented at the Univ. of Colorado. International Space Symposium for Flight Dynamics, 2014.
[11] T. Kelecy, E. Gerber, S. Akram, and J. Paffett, “Characterization of resident space object states using functional data analysis,” *The Journal of the Astronautical Sciences*, vol. 69, no. 2, pp. 627–649, 2022.
[12] K. A. Rush, “An application of the unscented Kalman filter for spacecraft attitude estimation on real and simulated light curve data,” 2020.
[13] A. Kembhavi and R. Pattnaik, “Machine learning in astronomy,” *Journal of Astrophysics and Astronomy*, vol. 43, no. 2, p. 76, 2022.
[14] M. Abubekerov and N. Y. Gostev, “High-precision calculation of the light curve and its interpretation,” *Astronomy & Astrophysics*, vol. 633, p. A96, 2020.
[15] O. Pimentel, P. A. Estevez, and F. Förster, “Deep attention-based supernovae classification of multiband light curves,” *The Astronomical Journal*, vol. 165, no. 1, p. 18, 2023.
[16] J. Faouzi, “Time series classification: A review of algorithms and implementations,” *Time Series Analysis-Recent Advances, New Perspectives and Applications*, p. 298, 2024.
[17] H.-Y. Liu, Z.-Z. Gao, Z.-H. Wang, and Y.-H. Deng, “Time series classification with shapelet and canonical features,” *Applied Sciences*, vol. 12, no. 17, p. 8685, 2022.
[18] Y. Tong *et al.*, “Technology investigation on time series classification and prediction,” *PeerJ Computer Science*, vol. 8, p. e982, 2022.
[19] E. Keogh, “Finding Repeated Structures in Time Series: Algorithms and Applications: A Unifying View of Time Series Motifs/Shapelets/Chains and Similar Primitives,” presented at the Proceedings of the 31st ACM SIGKDD Conference on Knowledge Discovery and Data Mining V. 2, 2025, pp. 6054–6062.
[20] A. Akhmetali *et al.*, “Classification of Variable Star Light Curves with Convolutional Neural Network,” *Galaxies*, vol. 12, no. 6, p. 75, 2024.
[21] R. Merino, P. Jara, B. Peralta, O. Nicolis, H. Lobel, and L. Caro, “Self-Supervised Learning Applied to Variable Star Semi-Supervised Classification Using LSTM and GRU Networks,” presented at the 2024 L Latin American Computer Conference (CLEI), IEEE, 2024, pp. 1–8.
[22] T. Xu *et al.*, “A Catalog of LAMOST Variable Sources Based on Time-domain Photometry of ZTF,” *The Astrophysical Journal Supplement Series*, vol. 259, no. 1, p. 11, 2022.

[23] M. Neira *et al.*, “MANTRA: A Machine-learning Reference Light-curve Data Set for Astronomical Transient Event Recognition,” *ApJS*, vol. 250, no. 1, p. 11, Sep. 2020, doi: 10.3847/1538-4365/aba267.
[24] B. T.-H. Tsang and W. C. Schultz, “Deep Neural Network Classifier for Variable Stars with Novelty Detection Capability,” *ApJL*, vol. 877, no. 2, p. L14, May 2019, doi: 10.3847/2041-8213/ab212c.
[25] P. R. McWhirter, A. Hussain, D. Al-Jumeily, I. A. Steele, and M. M. B. R. Vellasco, “Classifying Periodic Astrophysical Phenomena from non-survey optimized variable-cadence observational data,” *Expert Systems with Applications*, vol. 131, pp. 94–115, Oct. 2019, doi: 10.1016/j.eswa.2019.04.035.
[26] G. Li, B. Choi, J. Xu, S. S. Bhowmick, K.-P. Chun, and G. L. H. Wong, “Efficient Shapelet Discovery for Time Series Classification (Extended Abstract),” in *2021 IEEE 37th International Conference on Data Engineering (ICDE)*, Apr. 2021, pp. 2336–2337. doi: 10.1109/ICDE51399.2021.00254.
[27] L. Robinson and C. Frueh, “Optimal light curve attitude inversion with measurement noise: two case studies,” presented at the Proceedings of the 9th European Conference on Space Debris, Bonn, Germany, 2025.
[28] S. Vatankhah, P. G. Lelièvre, and J. Giraud, “Review of Advancements in Geometry-Based Inversion of Geophysical Data Sets,” *Surveys in Geophysics*, vol. 46, no. 5, pp. 973–1018, 2025.
[29] L. Robinson and C. Frueh, “Light curve inversion for reliable shape reconstruction of human-made space objects,” presented at the Proceedings of the 32nd AIAA/AAS Astrodynamics Specialist Conference, AIAA Reston, VA, 2022, pp. 1–19.
[30] Y. Zhao, H. Gao, and Z. Zong, “Satellite Attitude Control Enhancement Method Integrating LSTM-EKF Forward Prediction,” presented at the 2025 2nd International Conference on Unmanned Systems and Automation Control (ICUSAC), IEEE, 2025, pp. 157–164.
[31] R. Linares, J. L. Crassidis, and M. K. Jah, “Particle filtering light curve based attitude estimation for non-resolved space objects,” *Advances in the Astronautical Sciences*, vol. 152, pp. 119–130, 2014.
[32] M. Howard, B. Klem, and J. Gorman, “Rso characterization with photometric data using machine learning,” 2015.
[33] R. Linares and R. Furfaro, “Space object classification using deep convolutional neural networks,” presented at the 2016 19th International Conference on Information Fusion (FUSION), IEEE, 2016, pp. 1140–1146.
[34] M. Hwang, V. Suthakar, R. Qashoa, R. S. Lee, and G. Sohn, “Light-Curve Classification of Resident Space Objects for Space Situational Awareness: A Scoping Review,” *Aerospace*, vol. 13, no. 3, p. 287, 2026.
[35] Y. Lu, H. Wang, Y. Zang, Z. Liao, Q. Ning, and Z. Yan, “Elaborate imaging simulation and validation of the space target based on surface fractal features,” *Optics Express*, vol. 33, no. 12, pp. 24813–24830, 2025.
[36] F. J. Masci *et al.*, “The zwicky transient facility: Data processing, products, and archive,” *Publications of the Astronomical Society of the Pacific*, vol. 131, no. 995, p. 018003, 2019.

Supplementary Files

This is a list of supplementary files associated with this preprint. Click to download.

- dataset.csv